

**The Fine Line between a Two-Phase and Solid-Solution Phase Transformation and Highly Mobile Phase Interfaces in Spinel  $\text{Li}_{4+x}\text{Ti}_5\text{O}_{12}$**

Ganapathy, Swapna; Vasileiadis, Alexandros; Heringa, Jouke R.; Wagemaker, Marnix

**DOI**

[10.1002/aenm.201601781](https://doi.org/10.1002/aenm.201601781)

**Publication date**

2017

**Document Version**

Accepted author manuscript

**Published in**

Advanced Energy Materials

**Citation (APA)**

Ganapathy, S., Vasileiadis, A., Heringa, J. R., & Wagemaker, M. (2017). The Fine Line between a Two-Phase and Solid-Solution Phase Transformation and Highly Mobile Phase Interfaces in Spinel  $\text{Li}_{4+x}\text{Ti}_5\text{O}_{12}$ . *Advanced Energy Materials*, Article 1601781. <https://doi.org/10.1002/aenm.201601781>

**Important note**

To cite this publication, please use the final published version (if applicable).  
Please check the document version above.

**Copyright**

Other than for strictly personal use, it is not permitted to download, forward or distribute the text or part of it, without the consent of the author(s) and/or copyright holder(s), unless the work is under an open content license such as Creative Commons.

**Takedown policy**

Please contact us and provide details if you believe this document breaches copyrights.  
We will remove access to the work immediately and investigate your claim.

# The fine line between a two-phase and solid-solution phase transformation and highly mobile phase interfaces in spinel $\text{Li}_{4+x}\text{Ti}_5\text{O}_{12}$

*Swapna Ganapathy†, Alexandros Vasileiadis†, Jouke R. Heringa and Marnix Wagemaker\**

Fundamental Aspects of Materials and Energy, Department of Radiation Science and Technology, Faculty of Applied Sciences, Delft University of Technology, Mekelweg 15, 2629 JB Delft, The Netherlands

† these authors contributed equally to this work

\*corresponding author e-mail: [m.wagemaker@tudelft.nl](mailto:m.wagemaker@tudelft.nl)

## Abstract

Phase transitions play a crucial role in Li-ion battery electrodes being decisive for both the power density and cycle life. The kinetic properties of phase transitions are relatively unexplored and the nature of the phase transition in defective spinel  $\text{Li}_{4+x}\text{Ti}_5\text{O}_{12}$  introduces a controversy as the very constant (dis)charge potential, associated with a first-order phase transition, appears to contradict the exceptionally high rate performance associated with a solid-solution reaction. With the present DFT study, a microscopic mechanism is put forward that provides deeper insight in this intriguing and technologically relevant material. The local substitution of Ti with Li in the spinel  $\text{Li}_{4+x}\text{Ti}_5\text{O}_{12}$  lattice stabilizes the phase boundaries that are introduced upon Li-ion insertion. This facilitates a sub-nanometer phase coexistence in equilibrium, which although very similar to a solid solution should be considered a true first-order phase transition. The resulting interfaces are predicted to be very mobile due to the high mobility of the Li-ions located at the interfaces. This highly mobile, almost liquid-like, sub-nanometer phase morphology is able to

respond very fast to non-equilibrium conditions during battery operation, explaining the excellent rate performance in combination with a first-order phase transition.

# 1 Introduction

Electrochemical energy storage in Li-ion batteries is a key technology for the development of portable electronics and electrical vehicles. In addition it is now considered as a storage media for bridging the difference between supply of renewable energy sources and the societal demand. The working principle of Li-ion batteries is based on the reversible insertion and extraction of Li-ions in the crystal structure of the positive and negative electrode materials. The nature of the phase transitions in the electrode materials induced by the insertion of Li-ions is of large practical importance for Li-ion battery performance as it affects both the cycle life and power density. First-order phase transitions result in an attractive flat electrode potential, the phase boundaries formed, however, are thought to be responsible for poor rate performance and typically lead to poor cycle performance by strain-induced mechanical failure. Interestingly, two intensively studied electrode materials, olivine  $\text{LiFePO}_4$ <sup>[1]</sup> and spinel  $\text{Li}_4\text{Ti}_5\text{O}_{12}$ <sup>[2a, b]</sup> appear to be exceptions, showing excellent rate performance in combination with a long cycle life. For olivine  $\text{LiFePO}_4$ , recent studies have provided first insights in the phase-transition kinetics of electrode materials. Metastable intermediate phases were observed, induced by the high (dis)charge rates<sup>[3a, b]</sup> and the first-order phase transition was predicted and observed to be bypassed.<sup>[4a, b, c, d, e, f]</sup> In addition, the phase transition morphology in individual grains was shown to depend on the (dis)charge rate.<sup>[4d]</sup> For spinel  $\text{Li}_4\text{Ti}_5\text{O}_{12}$ , the fundamental nature of the first-order phase transition is unclear even at equilibrium. This is demonstrated by the fundamentally different phase transition behaviour that has been reported: (1) a complete solid solution,<sup>[5]</sup> (2) a nano-scale phase separated system<sup>[6a, b, c]</sup> or (3) a macroscopically phase separated system<sup>[7a, b]</sup>. Herein, the experimental difficulty is to distinguish between the structurally very similar  $\text{Li}_4\text{Ti}_5\text{O}_{12}$  and  $\text{Li}_7\text{Ti}_5\text{O}_{12}$  endmember crystalline lattices.<sup>[2a, b, 6a, 7a]</sup> Upon lithiation the spinel  $\text{Li}_4\text{Ti}_5\text{O}_{12}$  endmember phase undergoes a phase

transition towards the rock-salt  $\text{Li}_7\text{Ti}_5\text{O}_{12}$  endmember phase while maintaining its symmetry with a volume change of only 0.2%.<sup>[2a, b, 7a, 8a, b, c, d]</sup> This so-called ‘zero-strain’ property allows the material to go through thousands of charge-discharge cycles with marginal capacity loss and also suggests that interfaces between the endmember phases,  $\text{Li}_4\text{Ti}_5\text{O}_{12}$  and  $\text{Li}_7\text{Ti}_5\text{O}_{12}$ , can be associated with a very small energy penalty<sup>[9]</sup> unlike in other Li-ion electrode materials such as anatase  $\text{TiO}_2$ <sup>[10]</sup> and  $\text{LiFePO}_4$ .<sup>[4b, 11]</sup> Although the very flat voltage profile suggests macroscopic two phase separation<sup>[7a]</sup> which is supported by electron microscopy studies,<sup>[7b]</sup> temperature-dependent X-ray diffraction advocates that intermediate  $\text{Li}_{4+x}\text{Ti}_5\text{O}_{12}$  compositions macroscopically phase separate below 80 K whereas at higher temperatures they segregate into nano-domains of the endmember phases<sup>[6a]</sup> which is supported by NMR experiments.<sup>[6b],[5]</sup> Several NMR studies indicate that the individual endmember phases have high barriers for Li-ion diffusion resulting in poor Li-ion mobility<sup>[5, 6b, 12a, b]</sup> which is supported by static DFT calculations,<sup>[13]</sup> whereas intermediate compositions display high Li-ion mobility<sup>[5, 6b, 12a, b]</sup> which is also supported by DFT calculations.<sup>[14]</sup> The assumption of macroscopic phase coexistence of the endmember phases poses a contradiction: how can a sum of two macroscopically phase separated poor Li-ion conductors give rise to the high mobility observed in intermediate compositions both with NMR<sup>11,13,18,19</sup> and macroscopic electrochemical techniques<sup>[15a, b, c, d, e]?</sup>

Using ab-initio DFT calculations this work aims at a fundamental understanding of the nature of the phase transition behavior and Li-ion kinetics in spinel  $\text{Li}_4\text{Ti}_5\text{O}_{12}$  and how this transition is correlated with the material’s excellent electrode performance in Li-ion batteries. The results reveal a crucial role for the interfaces between the two endmember phases, the abundant existence of which is facilitated by the partial replacement of Ti with Li. The intimate mixing of sub-nanometer domains of the endmember phases structurally appears as a solid solution, however it should be considered as a first-order phase transition, a consequence of the

very small energy associated with the coherent interfaces. Molecular dynamics simulations display ultra-fast interface kinetics of the sub-nanometer phase separated system driving the very high Li-ion mobility in the spinel  $\text{Li}_{4+x}\text{Ti}_5\text{O}_{12}$  lattice. The nature of the interfaces explains the contradicting observations and the excellent rate performance of this intriguing material, giving insight in the relation between atomic scale properties and excellent Li-ion battery performance.

## 2 Results and Discussion

### 2.1 Thermodynamics of Li-ions in $\text{Li}_4\text{Ti}_5\text{O}_{12}$

The use of pure spinel  $\text{Li}_x\text{TiO}_2$  and defective spinel  $\text{Li}_{4+x}\text{Ti}_5\text{O}_{12}$  as electrode materials in Li-ion batteries relies on its ability to store Li-ions at two distinct crystallographic sites, the tetrahedral  $8a$  site, referred to as  $\text{Li}^{8a}$ , and the octahedral  $16c$  site, referred to as  $\text{Li}^{16c}$ . Additionally in spinel  $\text{Li}_{4+x}\text{Ti}_5\text{O}_{12}$  Li-ions reside on the Ti ( $16d$ ) sub-lattice in a ratio of 1:5 Li:Ti, referred to as  $\text{Li}^{16d}$ . These Li-ions are strongly bonded and therefore do not participate in the Li-ion insertion and extraction during battery operation. Their presence ascertains almost identical lattice parameters for the  $\text{Li}_4\text{Ti}_5\text{O}_{12}$  and  $\text{Li}_7\text{Ti}_5\text{O}_{12}$  endmembers, which is in turn responsible for the zero-strain property.<sup>[8a]</sup> We start with predicting the distribution of the electrochemically inactive Li-ions over the Ti ( $16d$ ) sub-lattice. This is achieved by calculating the lowest energy  $\text{Li}^{16d} - \text{Ti}^{16d}$  configuration, that will serve as a starting point considering the Li-vacancy energetics on the electrochemically active Li  $8a$  and  $16c$  sub-lattices. The Li–Ti disorder on the  $16d$  sub-lattice is calculated in both  $\text{Li}_4\text{Ti}_5\text{O}_{12}$  and  $\text{Li}_7\text{Ti}_5\text{O}_{12}$  endmember phases, by using a three-fold primitive cell in the smallest supercell, which is the smallest supercell having the correct stoichiometry. For the 1:5 Li:Ti ratio this results in 19 symmetrically distinct configurations. The resulting total energies of these configurations after ionic relaxation, calculated using the generalized gradient approximation (GGA) in density functional theory (DFT),<sup>[16a, b, c]</sup> are shown in **Figure 1a**. All

calculations were performed without considering spin polarization because this does not change the energies significantly<sup>[17]</sup> indicating that magnetization does not play a significant role in the energetics of spinel  $\text{Li}_{4+x}\text{Ti}_5\text{O}_{12}$ . The two lowest  $\text{Li}^{16d} - \text{Ti}^{16d}$  energy configurations in  $\text{Li}_4\text{Ti}_5\text{O}_{12}$ , shown in **Figure 1b/c**, are identical to the two lowest  $\text{Li}^{16d} - \text{Ti}^{16d}$  energy configurations in  $\text{Li}_7\text{Ti}_5\text{O}_{12}$ .

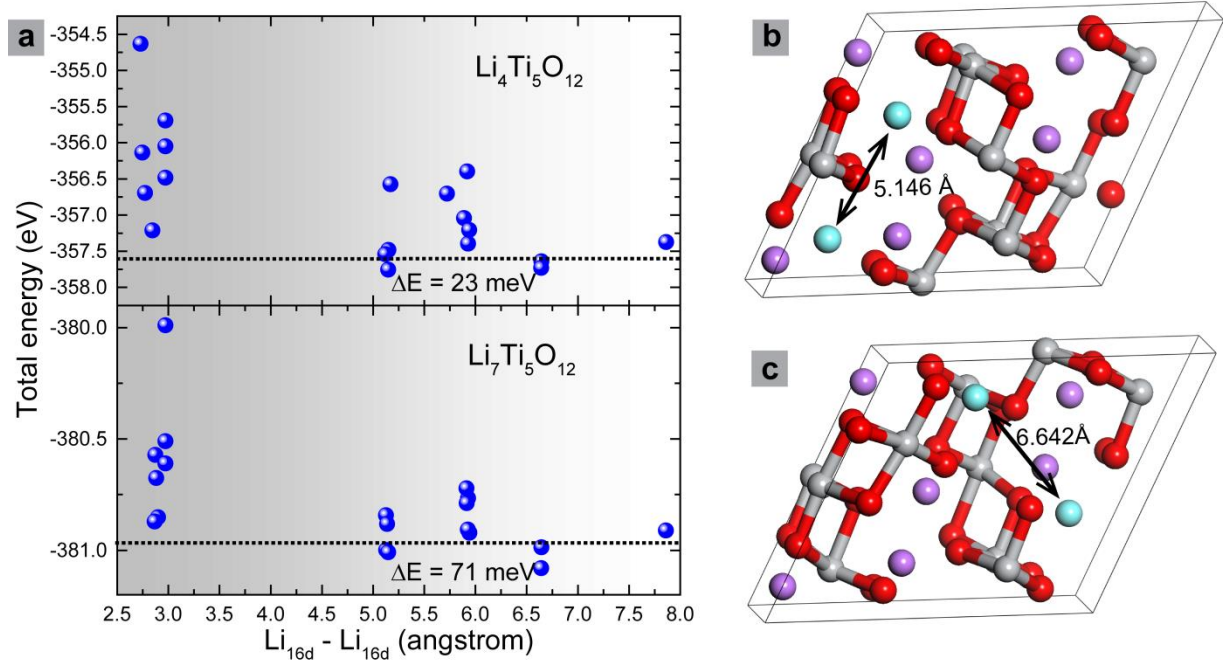


**Figure 1** (a) Total energy of all possible arrangements of Li and Ti (ratio 1:5) on the  $16d$  sublattice after relaxation in both endmembers stoichiometry's  $\text{Li}_4\text{Ti}_5\text{O}_{12}$  (supercell  $\text{Li}_6^{8a}[\text{Li}_2\text{Ti}_{10}]^{16d}\text{O}_{24}$ ) and  $\text{Li}_7\text{Ti}_5\text{O}_{12}$  (supercell  $\text{Li}_{12}^{16c}[\text{Li}_2\text{Ti}_{10}]^{16d}\text{O}_{24}$ ). (b)/(c) The two lowest energy configurations of  $\text{Li}_4\text{Ti}_5\text{O}_{12}$  obtained from (a). The cyan, purple, grey, and red spheres represent  $\text{Li}^{16d}$ ,  $\text{Li}^{8a}$ , Ti and O atoms respectively.

Analysis of the various  $\text{Li}^{16d} - \text{Ti}^{16d}$  configurations reveals that the energy systematically increases with decreasing  $\text{Li}^{16d} - \text{Li}^{16d}$  distance. A small  $\text{Li}^{16d} - \text{Li}^{16d}$  distance introduces a repulsive energy (the minimum  $16d-16d$  distance is 2.974 Å) explaining why the maximum  $\text{Li}^{16d} - \text{Li}^{16d}$  distances,

5.146 Å and 6.642 Å, results in the lowest total energy. The energy difference between the two lowest energy configurations is small, amounting to 23 meV and 71 meV for the  $\text{Li}_8\text{Ti}_{10}\text{O}_{24}$  and the  $\text{Li}_{14}\text{Ti}_{10}\text{O}_{24}$  endmember supercells respectively. This indicates, that, in practice, the  $\text{Li}^{16d} - \text{Ti}^{16d}$  disorder may consist of a mixture of these two configurations.

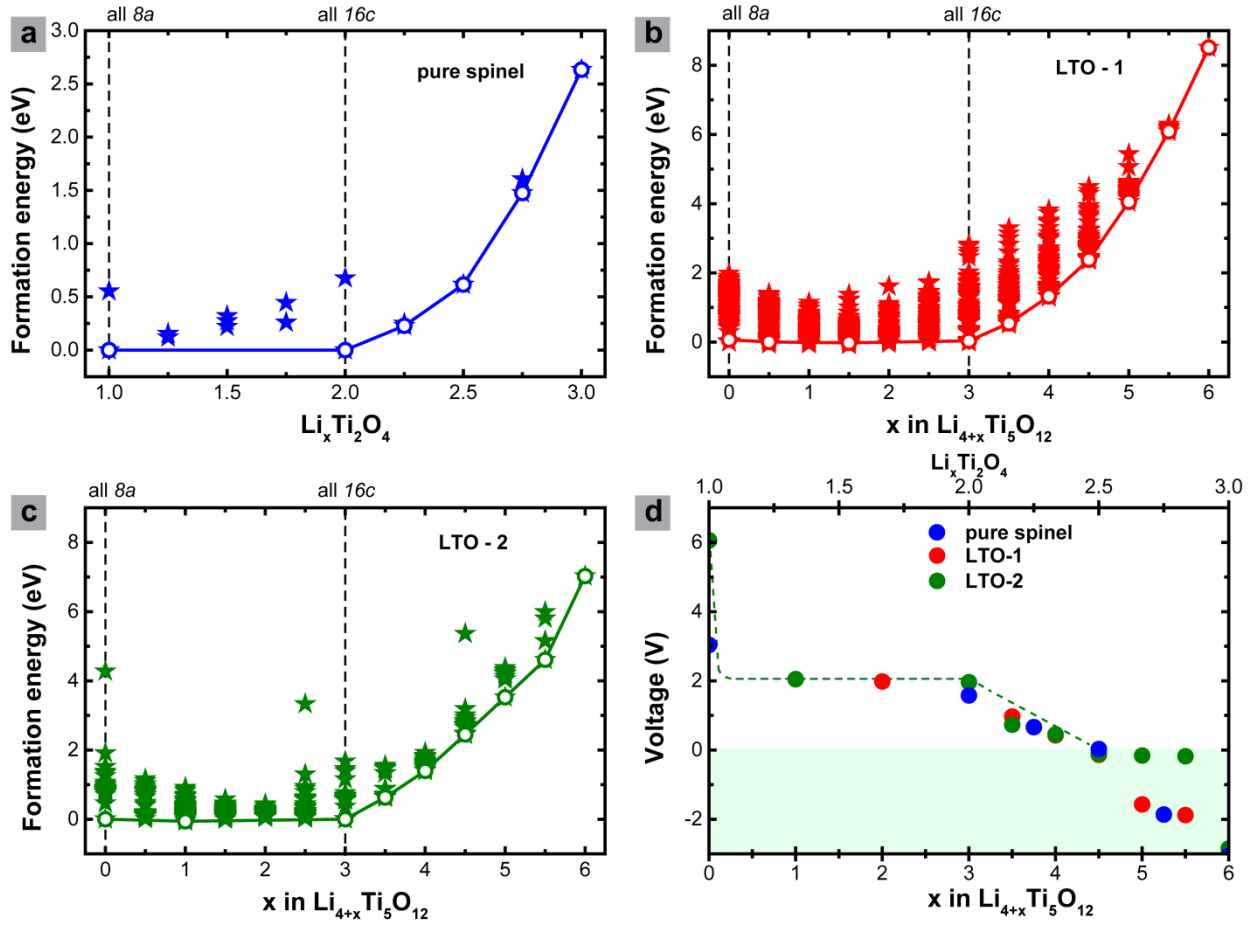


**Figure 2** Formation energies (stars) of (a) pure spinel  $\text{Li}_x\text{Ti}_2\text{O}_4$ , (b) LTO-1 and (c) LTO-2 configurations. Formation energies were determined per formula unit of  $\text{Li}_x\text{Ti}_2\text{O}_4$  and  $\text{Li}_{4+x}\text{Ti}_5\text{O}_{12}$  respectively. The bold line represents the convex hull comprised of the most stable ground states (hollow circles) that were determined in each case. (d) Insertion voltages determined for the pure  $\text{Li}_x\text{Ti}_2\text{O}_4$  and defective spinel  $\text{Li}_{4+x}\text{Ti}_5\text{O}_{12}$  from the total energies between consecutive points ( $\text{Li}$ -configurations) on the convex hull at 0 K. The dotted line in (d) is a guide to the eye.

We shall refer to the two different low-energy  $16d$  sub-lattice configurations as LTO-1 ( $\text{Li}^{16d} - \text{Li}^{16d}$  distance 5.146 Å) shown in **Figure 1b** and LTO-2 ( $\text{Li}^{16d} - \text{Li}^{16d}$  distance 6.642 Å) shown in **Figure 1c**. Given the small difference in ground state energy of the LTO-1 and LTO-2 configurations, the lithium-vacancy energetics on the  $8a$  and  $16c$  sub-lattices is calculated for both starting structures, using the initial part of the code for cluster expansion developed by Van de Ven and co-workers to obtain symmetrically unique configurations.<sup>[18a, b, c]</sup> Because the  $\text{Li}^{16d}$  ions do not participate in the insertion/extraction reaction during battery operation, the configuration of these ions as well as the O and Ti atoms is fixed (though the ionic positions are relaxed during the energy minimizations). For comparative purposes also the previously reported<sup>[17, 19]</sup> lithium-vacancy energetics on the  $8a$  and  $16c$  sub-lattices in pure spinel  $\text{Li}_x\text{Ti}_2\text{O}_4$  are calculated.

Putting vacancies in the pure spinel primitive cell on the  $8a$  and  $16c$  sub lattices results in 24 symmetrically distinct lithium-vacancy configurations. The large size of the  $\text{Li}_{4+x}\text{Ti}_5\text{O}_{12}$  (LTO-1/2) supercells (three times the primitive cell) and the reduced local symmetry, introduced by the  $\text{Li}^{16d}$  atoms, results in a much larger amount of symmetrically distinct lithium-vacancy configurations on the  $8a$  and  $16c$  sub-lattices of which we have considered 2653 in LTO-1 and 1490 in LTO-2. In **Figures 2a-c** the formation enthalpies per formula unit  $\text{Li}_x\text{Ti}_2\text{O}_4$  ( $1 \leq x \leq 2$ ) and  $\text{Li}_{4+x}\text{Ti}_5\text{O}_{12}$  ( $0 \leq x \leq 3$ ) for all calculated Li-vacancy arrangements, reflecting the relative stability of the different configurations (the formation enthalpies of the complete compositional range are provided in the **Supporting Information A, Figure S1**). The formation enthalpy for the defective spinel can be defined as:

$$E_{form} = E_{\text{Li}_{4+x}\text{Ti}_5\text{O}_{12}} - \frac{x}{3} E_{\text{Li}_7\text{Ti}_5\text{O}_{12}} - \left(1 - \frac{x}{3}\right) E_{\text{Li}_4\text{Ti}_5\text{O}_{12}}$$

Where  $E$  is the energy of a specific Li-vacancy arrangement at a concentration  $x$ ,  $E_{\text{Li}_7\text{Ti}_5\text{O}_{12}}$  is the energy of the endmember phase where all octahedral  $16c$  sites are occupied and  $E_{\text{Li}_4\text{Ti}_5\text{O}_{12}}$  is the energy of the endmember phase where all tetrahedral  $8a$  sites are occupied. The formation enthalpy of the pure spinel is described in detail elsewhere.<sup>[17, 19]</sup> Considering the formation enthalpies makes it possible to study the relative stability of the different configurations, and thereby predicting the thermodynamic path upon (de)lithiation. The lines in **Figures 2a-c**, represent part of the convex-hull which is constructed by connecting a line between the most stable (ground state) structures at 0 K as a function of Li composition. Before considering LTO-1 and LTO-2 it is illustrative to start with the formation enthalpies of the pure spinel phase shown in **Figure 2a**. Starting at the  $\text{Li}_1\text{Ti}_2\text{O}_4$  ground state, where the  $8a$  sub-lattice is completely occupied by Li-ions, additional Li-ion insertion results in configurations with a mixed  $\text{Li}^{8a}/\text{Li}^{16c}$  occupancy, before reaching the  $\text{Li}_2\text{Ti}_2\text{O}_4$  ground state, where all  $16c$  sites are occupied. The formation energies of these mixed  $\text{Li}^{8a}/\text{Li}^{16c}$  configurations are positioned significantly above the convex hull connecting the  $\text{Li}_1\text{Ti}_2\text{O}_4$  and  $\text{Li}_2\text{Ti}_2\text{O}_4$  ground states indicating a thermodynamic driving force for the first-order phase transition between these ground states in agreement with experimental observations and previous calculations.<sup>[15c],39</sup> **Figures 2b** and **2c** show the formation enthalpies of both LTO-1 and LTO-2 for the same compositional range, from lithium occupying all  $8a$  sites in  $\text{Li}_4\text{Ti}_5\text{O}_{12}$  to lithium occupying all  $16c$  sites in  $\text{Li}_7\text{Ti}_5\text{O}_{12}$ . Comparison shows that LTO-1 and LTO-2 have a very similar ground state energies upon Li-ion insertion in the  $8a$  and  $16c$  sub-lattices that differs fundamentally from those predicted for pure spinel. In contrast to pure spinel, both LTO-1 and LTO-2 result in several mixed  $\text{Li}^{8a}/\text{Li}^{16c}$  configurations ( $0 \leq x \leq 3$ ) that have a formation enthalpy very close and even positioned on the convex hull (two additional for LTO-1 and one for LTO-2). This implies that in spinel  $\text{Li}_{4+x}\text{Ti}_5\text{O}_{12}$  configurations with mixed Li-

ion occupancy of  $8a$  and  $16c$  sites are relatively stable and likely to occur in practice. This in contrast to pure spinel  $\text{Li}_{1+x}\text{Ti}_2\text{O}_4$  where the large formation energy of these mixed  $\text{Li}^{8a}/\text{Li}^{16c}$  configurations provides a driving force towards macroscopic phase separation in domains of occupied  $8a$  sites and domains of occupied  $16c$  sites.

The voltage profile in **Figure 2d** is determined from the most stable consecutive ground state configurations, positioned on the convex hull, shown for the complete concentration range in the **Supporting Information A, Figure S1**. As expected, the similar convex hull of LTO-1 and LTO-2 result in very similar voltage profiles. For compositions between  $\text{Li}_7\text{Ti}_5\text{O}_{12}$  and  $\text{Li}_{8.4}\text{Ti}_5\text{O}_{12}$ , in addition to all the  $16c$  sites being occupied, additional Li-ions occupy the  $8a$  sites, causing distortions in the neighbouring  $\text{TiO}_6$  octahedra, observed both in LTO-1 and LTO-2, in agreement with previous theoretical studies.<sup>[20]</sup> Compositions in excess of  $\text{Li}_7\text{Ti}_5\text{O}_{12}$  have also been observed experimentally for nano sized LTO, in agreement with our observations wherein in addition to full  $16c$  occupancy; partial  $8a$  occupancy was reported using neutron diffraction.<sup>[21]</sup> LTO-1 and LTO-2 differ only significantly at compositions exceeding  $\text{Li}_{8.4}\text{Ti}_5\text{O}_{12}$ , at which point the voltages obtained for Li insertion are negative. The negative voltage indicates that the free energy is lower than that of metallic lithium and hence Li-plating is preferred over exceeding the  $\text{Li}_{8.4}\text{Ti}_5\text{O}_{12}$  composition. This is in good agreement with values predicted by Zhong and co-workers<sup>[20]</sup> and those obtained via chemical/electrochemical insertion in nano  $\text{Li}_{4+x}\text{Ti}_5\text{O}_{12}$ .<sup>[21, 22]</sup> For pure spinel  $\text{Li}_x\text{Ti}_2\text{O}_4$  the voltage profiles reported in the literature have been obtained by performing Monte Carlo simulations at 300 K based on a cluster expansion using the DFT energies<sup>[17, 19]</sup> whereas at present we report the voltage curve solely based on the ground state enthalpies, and therefore the configurational entropy is not included. In the composition range  $0 \leq x \leq 3$  in  $\text{Li}_{4+x}\text{Ti}_5\text{O}_{12}$  the voltages are predicted to be almost constant at  $2.00 \pm 0.04$  V, both for LTO-1 and LTO-2. This calculated value is higher than the experimentally observed plateau

voltage which is  $\approx 1.55$  V vs. metallic Li.<sup>[7a, 8c]</sup> These discrepancies between calculated and experimental insertion voltages are often reported using DFT calculations,<sup>[23a, b]</sup> and do not influence any trends in the voltage drop observed as a function of increased Li-concentration.

Although both pure spinel  $\text{Li}_x\text{Ti}_2\text{O}_4$  and defective  $\text{Li}_{4+x}\text{Ti}_5\text{O}_{12}$  display a constant voltage plateau, the underlying structural changes are very different. In the  $\text{Li}_x\text{Ti}_2\text{O}_4$  the formation energies in **Figure 2a** indicate that it is due to a macroscopic phase separation, driven by the large energy penalty of mixed  $\text{Li}^{8a}/\text{Li}^{16c}$  sites, in practice leading to domains where Li-ions occupy the  $8a$  sites and domains where the Li-ions occupy  $16c$  sites thereby avoiding the mixed -  $\text{Li}^{8a}/\text{Li}^{16c}$  site occupancy. However in  $\text{Li}_{4+x}\text{Ti}_5\text{O}_{12}$ , a number of configurations with mixed -  $\text{Li}^{8a}/\text{Li}^{16c}$  site occupancy are close or even on the convex-hull, indicating that the material will transform from  $\text{Li}_4\text{Ti}_5\text{O}_{12}$  to  $\text{Li}_7\text{Ti}_5\text{O}_{12}$  via these  $\text{Li}^{8a}/\text{Li}^{16c}$  configurations. Because the only difference between  $\text{Li}_x\text{Ti}_2\text{O}_4$  and  $\text{Li}_{4+x}\text{Ti}_5\text{O}_{12}$  is the presence of Li-ions on the Ti  $16d$  sub-lattice, these ions appear to stabilize the mixed  $\text{Li}^{8a}/\text{Li}^{16c}$  site occupancy.

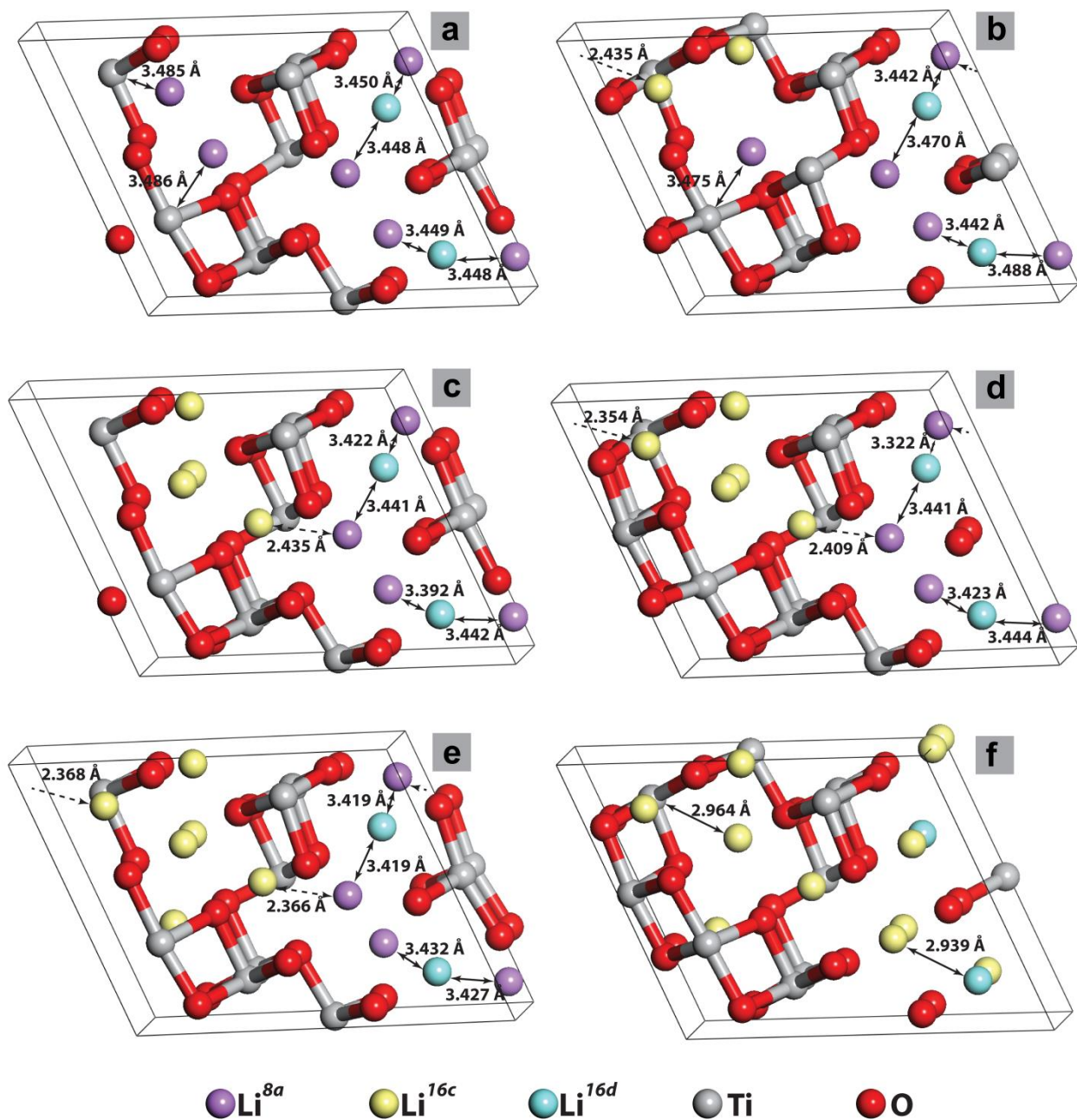


**Figure 3** Structures corresponding to the lowest energy configurations of LTO-1 where panels (a) – (f) correspond to  $\text{Li}_4\text{Ti}_5\text{O}_{12}$ ,  $\text{Li}_{4.5}\text{Ti}_5\text{O}_{12}$ ,  $\text{Li}_5\text{Ti}_5\text{O}_{12}$ ,  $\text{Li}_{5.5}\text{Ti}_5\text{O}_{12}$ ,  $\text{Li}_6\text{Ti}_5\text{O}_{12}$ , and  $\text{Li}_{6.5}\text{Ti}_5\text{O}_{12}$  respectively some of which fall on the convex hull. The red and grey balls correspond to O and Ti, while the cyan, violet, and yellow balls correspond to Li at the 16d, 8a, and 16c sites respectively.

To gain insight in this mechanism the  $\text{Li}_{4+x}\text{Ti}_5\text{O}_{12}$  lowest energy configurations, three of which are positioned on the convex hull, as shown in **Figure 2b**, are studied in more detail. The structure of the all  $\text{Li}^{8a}$  occupied,  $\text{Li}_4\text{Ti}_5\text{O}_{12}$  of LTO-1, shown in **Figure 3a**, has relatively short  $\text{Li}^{8a} - \text{Li}^{16d}$  distances (3.448 – 3.450 Å) as compared to the  $\text{Li}^{8a} - \text{Ti}^{16d}$  distances (3.485–3.486 Å). The mixed  $\text{Li}^{8a}/\text{Li}^{16c}$  occupancy is observed in **Figures 3b-e**, corresponding to LTO-1 configurations with compositions of  $\text{Li}_{4.5}\text{Ti}_5\text{O}_{12}$  up to  $\text{Li}_6\text{Ti}_5\text{O}_{12}$ , where it is observed that the nearest  $\text{Li}^{16c} - \text{Li}^{8a}$  pairs occur near the  $\text{Li}^{16d}$  position. This indicates that the  $\text{Li}^{16d}$  atom stabilizes the  $\text{Li}^{8a} - \text{Li}^{16c}$  nearest neighbors, albeit up to a certain maximum Li concentration. When the composition exceeds  $\text{Li}_6\text{Ti}_5\text{O}_{12}$ , the  $\text{Li}^{8a}$  ions move to neighboring  $16c$  sites as observed in **Figure 3f**. In pure spinel the nearest  $\text{Li}^{8a} - \text{Li}^{16c}$  neighbors would result in a interatomic distance of 1.82 Å<sup>[19]</sup> and hence a large Coulombic repulsion making these configurations energetically unfavorable. In LTO the nearby  $\text{Li}^{16d}$  sites allow the  $\text{Li}^{8a} - \text{Li}^{16c}$  distance to relax to a distance in the range of 2.354 – 2.435 Å (lowering the Coulombic repulsion) as shown in **Figures 3d-e**. Configurations with a smaller  $\text{Li}^{8a} - \text{Li}^{16c}$  distance result in a higher formation enthalpy. For example the composition  $\text{Li}_{5.5}\text{Ti}_5\text{O}_{12}$  of LTO-1, where the lowest energy configuration has been depicted in **Figure 3d**, has a  $\text{Li}^{8a} - \text{Li}^{16c}$  distance between 2.354 – 2.435 Å. At the same composition the configuration with a 200 meV/Li higher formation enthalpy, shown in the **Supporting Information A (Figure S2)**, contains several  $\text{Li}^{8a} - \text{Li}^{16c}$  nearest neighbors, however, of which all but one have a  $\text{Li}^{16d}$  adjoining atom. Because the  $\text{Li}^{8a}$  atoms are not able to relax towards the  $\text{Ti}^{16d}$  atoms the  $\text{Li}^{8a} - \text{Li}^{16c}$  distances are relatively small (1.986 – 2.122 Å) which is responsible for the higher formation enthalpy. The same stabilization mechanism is observed in LTO-2.

A consequence of the nearest  $\text{Li}^{8a} - \text{Li}^{16c}$  stabilization adjacent to  $\text{Li}^{16d}$  atoms in spinel  $\text{Li}_{4+x}\text{Ti}_5\text{O}_{12}$  is that the phase separation between domains of  $8a$  occupancy and  $16c$  occupancy,

representing the first-order phase transition, is mixed on a sub-nanometer length scale in contrast to pure spinel.

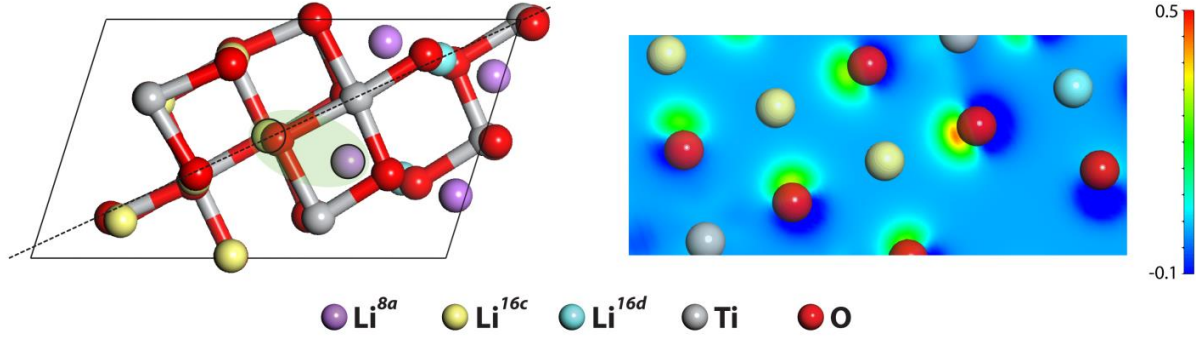


**Figure 4** Lowest energy  $\text{Li}_6\text{Ti}_5\text{O}_{12}$  configuration of LTO-1 (Left) and a cross section of the difference in charge density (Right) between the  $\text{Li}_6\text{Ti}_5\text{O}_{12}$  configuration and the  $\text{Li}_1\text{Ti}_4\text{O}_{12}$  configuration consisting only of  $\text{Li}^{16d}$ . The cross-sectional plane chosen passes through the  $\text{Li}^{16d} - \text{Li}^{16c} - \text{Ti}^{16d}$  atoms indicated by the dotted line. Of these atoms the  $\text{Li}^{16c}$  forms part of the nearest neighbor  $\text{Li}^{8a} - \text{Li}^{16c}$  pair denoted by the green shaded oval.

The stabilization mechanism of adjoining  $\text{Li}^{8a}$  and  $\text{Li}^{16c}$  is further investigated by considering the difference in valence electron density upon lithium addition between the most stable  $\text{Li}_6\text{Ti}_5\text{O}_{12}$  (LTO-1) and  $\text{Li}_1\text{Ti}_4\text{O}_{12}$  (LTO-1) configurations shown in **Figure 4**. From a cross section of the charge density difference it is observed that upon lithium addition, the electron density is donated to the 2p-O and 3d-Ti orbitals of the neighboring O and Ti atoms. Consequentially, the  $\text{Li}^{16c}$  atom neighboring the  $\text{Li}^{8a}$  (nearest to the  $\text{Li}^{16d}$ ) seen in the left panel of **Figure 4** is better shielded by the electrons residing in the O orbitals in its vicinity in comparison with other  $\text{Li}^{16c}$  atoms, with a larger charge density being transferred to the oxygen atom adjacent to the  $\text{Li}^{16d}$ . In addition to the larger  $\text{Li}^{8a} - \text{Li}^{16c}$  nearest neighbor distances allowed in the vicinity of a  $\text{Li}^{16d}$ , the electron density screening is responsible for the stabilization of the nearest  $\text{Li}^{8a}$  and

$Li^{16c}$  neighbors in spinel  $Li_{4+x}Ti_5O_{12}$ , resulting in the formation of sub-nanometer  $8a$ -rich and  $16c$ -rich domains.

## 2.2 Kinetics of Li-ions in $Li_4Ti_5O_{12}$ by Molecular Dynamics simulations

To investigate the kinetics of the Li-ions on the  $8a$  and  $16c$  sub-lattice Molecular Dynamics (MD) simulations were performed using DFT for intermediate compositions  $0 < x < 3$  in spinel  $Li_{4+x}Ti_5O_{12}$  hosting a mixture of  $8a$  and  $16c$  site occupancies. A  $2 \times 1 \times 2$  supercell was constructed with an initial (001) orientation of the interface between the domains of  $Li^{8a}$  and  $Li^{16c}$  occupancy, as shown in **Figure 5**, which was suggested to be a preferential interface orientation by TEM<sup>[7b]</sup> and static (0 K) DFT calculations<sup>[9]</sup>. Such sharp coherent interfaces, separating domains of  $Li^{8a}$  and  $Li^{16c}$ , were observed using electron microscopy<sup>[6c]</sup> reporting a small interface width of only a few Angstroms. At the (001) interface one layer of  $8a$  positions and  $16c$  positions is purposely left unoccupied, , to create a space for the interface to relax during the MD simulations, see **Figure 5**. The periodic boundary conditions introduce a second interface between the  $Li^{8a}$  and  $Li^{16c}$  domains also with the (001) orientation connecting the bottom of the supercell with the top, in this case introducing nearest  $Li^{8a}$  -  $Li^{16c}$  neighbors. Several supercell configurations that differ in size and stoichiometry were simulated for a calculation time of up to 200 pico seconds for a wide range of temperatures (300 to 600K), see **Supporting Information B**.

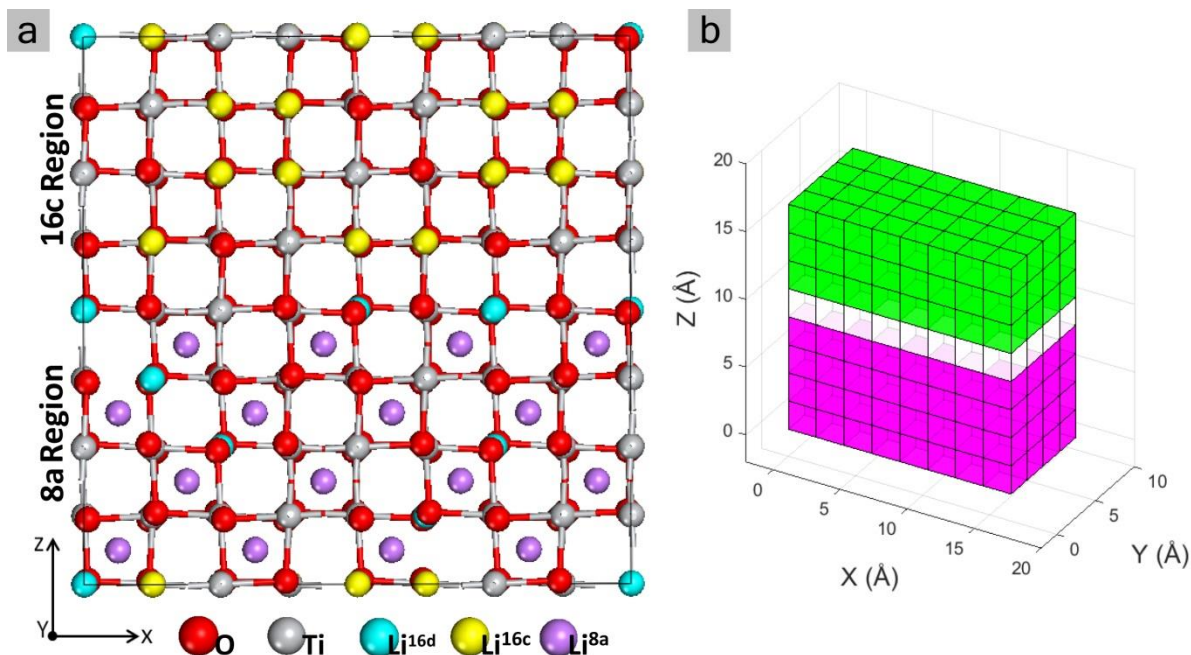


**Figure 5.** (a) 2x1x2 LTO supercell, starting point of the MD simulations. (b) 3D representation of the phase separated initial supercell: in green the Li-rich endmember ( $\text{Li}_7\text{Ti}_5\text{O}_{12}$ ) phase where all electrochemically active Li-ions occupy the 16c sites and in purple the Li-poor endmember ( $\text{Li}_4\text{Ti}_5\text{O}_{12}$ ) phase where all electrochemically active ions occupy the 8a sites. The dimensions of the supercell are  $1.67 \cdot 0.83 \cdot 1.67 \text{ nm}^3$  and the DFT calculations are performed under periodic boundary conditions.

During the first 2 ps (the initial stage of the MD simulations) the supercell shown in **Figure 5** immediately relaxes at the interfaces towards a variety of local  $\text{Li}^{8a} - \text{Li}^{16c} - \text{Li}^{16d}$  configurations, between which it fluctuates. These local configurations are very similar to the ground state configurations predicted by the static DFT calculations in the previous section where nearest  $\text{Li}^{8a} - \text{Li}^{16c}$  neighbors were shown to be stabilized by adjacent  $\text{Li}^{16d}$  atoms, see **Figures 3c-e**. The kinetics of the local configurations will be discussed in detail in a following paragraph. After the initial 2 ps the MD simulations show a highly mobile, liquid like, interface and domain

structure moving through the crystal lattice as shown in **Figure 6**. MD-simulations of the same supercell at different temperatures show similar results, however differing in the exact evolution of the morphology indicating the random character of the mobile domain interface (**Supporting Information C**).

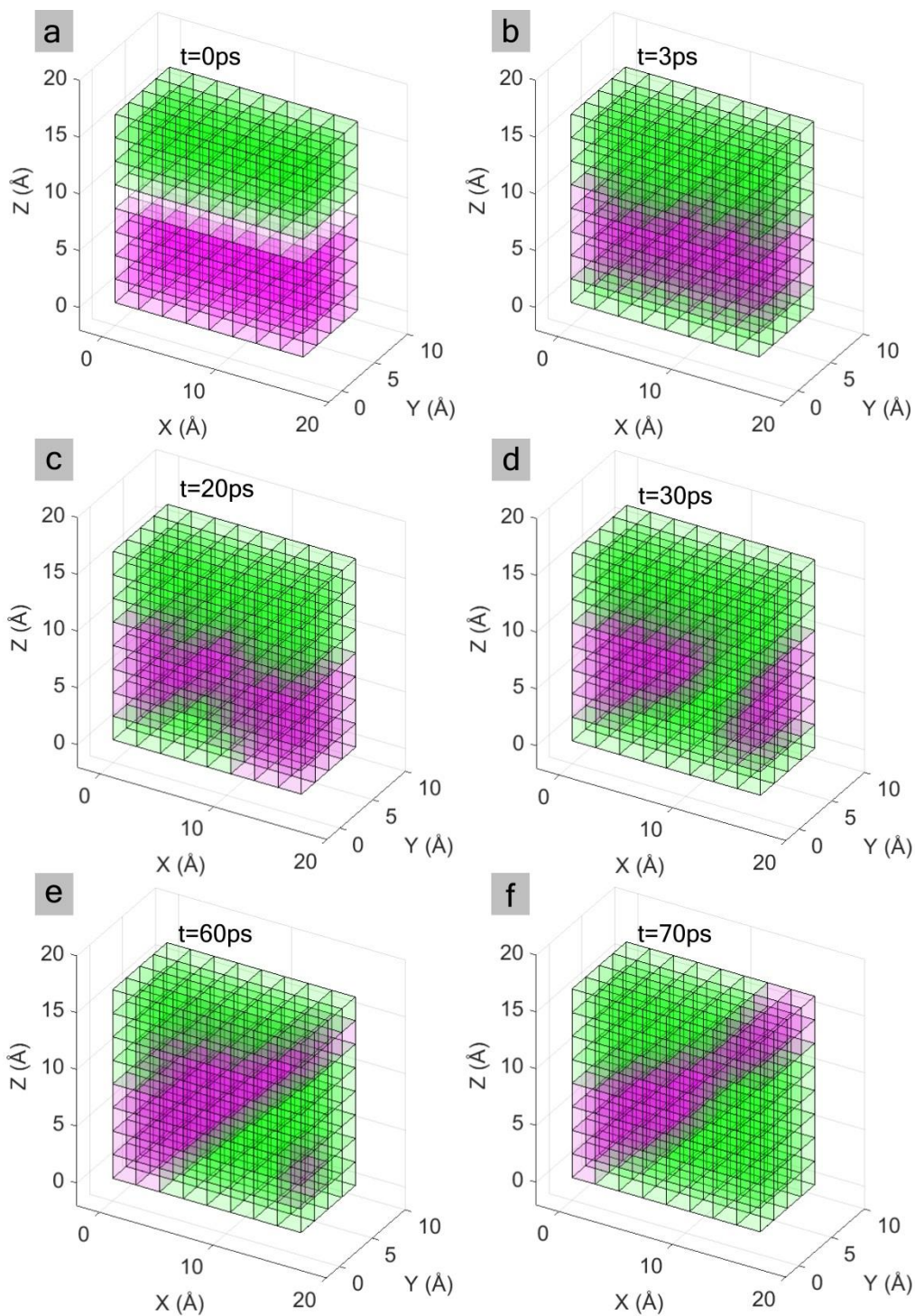


**Figure 6.** Snapshots of the phase morphology during the MD simulation showing the evolution of the Li-poor endmember ( $\text{Li}^{8a}$ ) and Li-rich endmember ( $\text{Li}^{16c}$ ) domains and the interface during 70 ps in the  $2 \times 1 \times 2$  supercell at 600 K.

The mobility of the  $\text{Li}^{8a}$  and  $\text{Li}^{16c}$  domain-interface morphology is the consequence of the high Li-ion mobility over the  $8a$  and  $16c$  sub-lattices. This is illustrated by **Figure 7a** and **7b** that display the relative positions of the  $8a$  and  $16c$  sites and the integrated Li-ion density during the first 100 out of the total 185 ps MD simulation at 520 K of a fraction of the supercell shown in **Figure 5**. It reveals the diagonal pathways connecting every  $8a$  site to another  $8a$  site in four directions, via a  $16c$  site, creating a 3D dimensional diffusional network. **Figure 7c** displays the mean square displacement (MSD) as a function of the MD simulation time. After approximately 100 ps the MSD reaches a plateau which is accompanied by an apparent stabilization of the interface in the (100) direction, see **Figure 7d**. For the cubic symmetry of spinel  $\text{Li}_{4+x}\text{Ti}_5\text{O}_{12}$  this is equivalent to the (010) and the (001) orientation from which the MD simulation was started. However, close examination at the atomic scale shows that locally no preferred interface exists. The diffusion of the Li-ions, and thereby the interface and domain mobility, is dictated by the  $\text{Li}^{16d}$  atoms, as will be discussed below. Given the stabilization of the MSD after approximately 100 ps, this should be considered as an equilibration of the system from the initial conditions shown in **Figure 5**. Therefore it is necessary to distinguish the Li-ion kinetics before and after the initial approximately 100 ps as this equilibration results in a MSD of the Li-ions, as observed in **Figure 7c**, whereas after 100 ps only local mobility is observed leading to fluctuations of the interface region between the  $\text{Li}^{8a}$  and  $\text{Li}^{16c}$  domains, see **Supporting Information D**. The stabilization of the MSD indicates that the MD system during the first 100 ps is not in equilibrium, a condition similar to that imposed during the operation of Li-ion battery electrodes where electrochemically driven insertion or extraction of Li-ions induces a non-equilibrium condition. We suggest that the diffusional relaxation mechanism is of interest for the understanding of the functioning of spinel  $\text{Li}_{4+x}\text{Ti}_5\text{O}_{12}$  as Li-ion battery electrode.

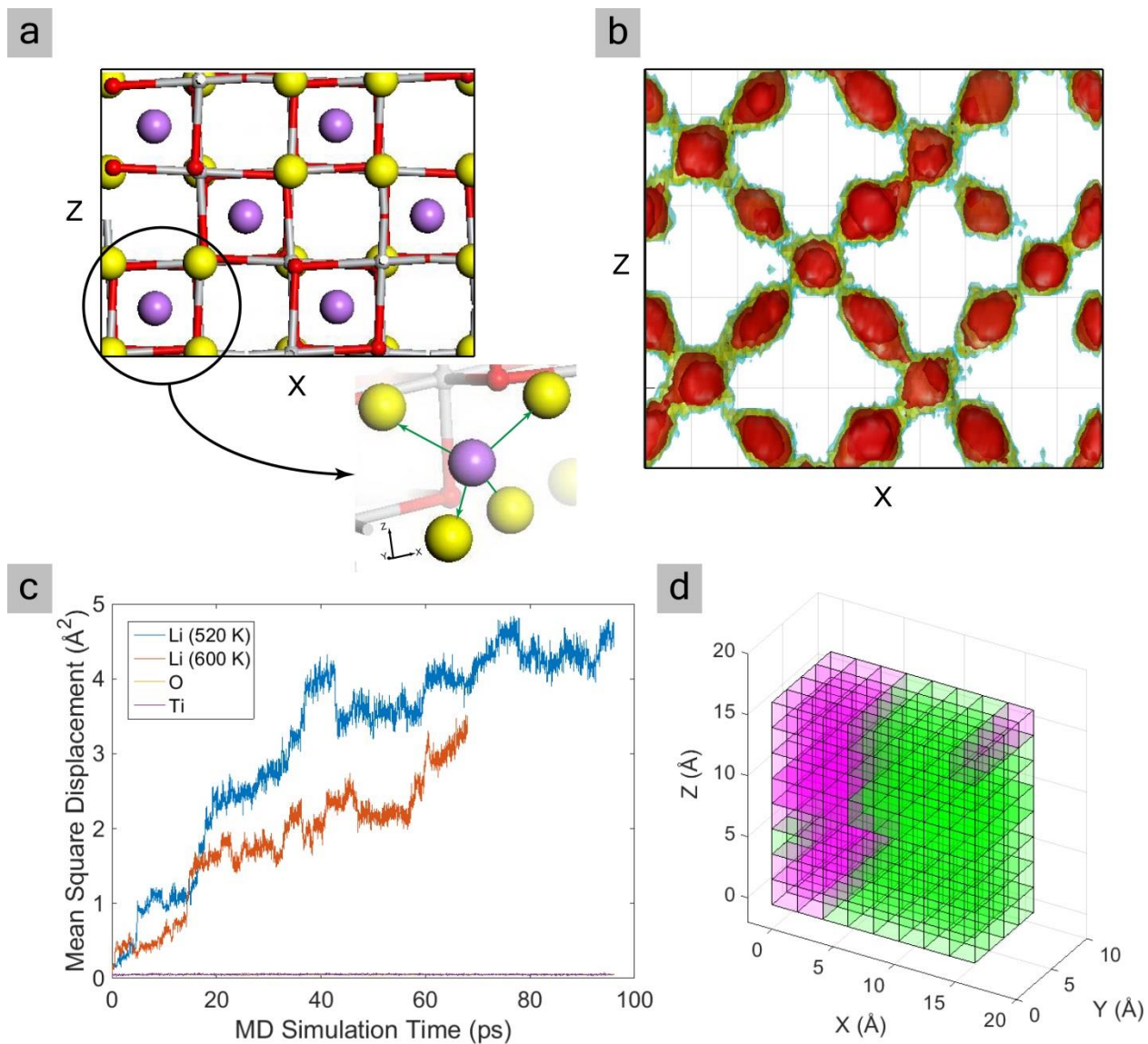


**Figure 7.** (a) Schematic representation of the all possible 8a and 16c sites in a fraction of the supercell and (b) Li-ion density plot integrated over the first 100 ps of the MD-simulation at 520 K, for comparison represented in the same fraction of the supercell shown in Figure 7(a), red colour represents high density, green represents lower Li-ion density indicating the characteristic diagonal (110) (011) (101) Li-ion diffusion pathways. (c) Mean square displacement (MSD) of all elements in the supercell for the first 100 ps out of the total 185 ps at

520 K and the total 70 ps at 600 K. (d) Representative 3D configuration for the configurations occurring after the first 100 ps.

From all possible Li-ion diffusional transitions (*16c-16c*, *8a-8a*, *16d-16c*, *16c-16d*, *16d-8a*, *8a-16d*, *8a-16c* and *16c-8a*) only the *16c-8a* and *8a-16c* transitions occur during the MD simulations, consistent with the high energy barriers for the other transitions measured with local probes and predicted by ab-initio calculations.<sup>[5, 6b, 12a, b, 13, 14]</sup> The most interesting observation is that the large majority of the transitions (>99.5%) takes place at interfaces *between* the  $Li^{8a}$ -domains and  $Li^{16c}$ -domains and practically no transitions occur *within* the  $Li^{8a}$ -domains and  $Li^{16c}$ -domains during the time of the MD simulations, the latter in agreement with experimental observations<sup>[5, 6b, 12a, b]</sup> pointing out sluggish diffusion at the endmember phases. This was further confirmed by MD simulations of the endmember phases  $Li_4Ti_5O_{12}$  ( $Li^{8a}$ ) and  $Li_7Ti_5O_{12}$  ( $Li^{16c}$ ) where no transitions were predicted at 600 K and up to 200 ps simulation time. This indicates that the high mobility of the Li-ions in spinel  $Li_4Ti_5O_{12}$ <sup>[5, 6b, 12b, 15a, d]</sup> should be attributed to high Li-ion mobility at the interfaces between the  $Li^{8a}$ -domains and  $Li^{16c}$ -domains. As concluded from the most stable configurations in **Figure 3**, the interfaces are stabilized by the  $Li^{16d}$  atoms resulting in sub-nanometer domains and hence a large abundance of these interfaces. As a consequence  $Li_{4+x}Ti_5O_{12}$  for the compositions  $0 < x < 3$  is an excellent Li-ion conductor due to the highly mobile and apparently abundant  $Li^{16d}$  stabilized interfaces. The rare conditions that lead to Li-ion transitions *within* the  $Li^{8a}$ -domains and  $Li^{16c}$ -domains (0.05% of all transitions) are analyzed in **Supporting Information E**. The energy barrier for the *8a-16c* and *16c-8a* transitions occurring at the domain interfaces are quantified by the mean jump rate  $\nu$  according to  $\nu = J/(Nt)$  where  $J$  represents the number of the *16c-8a* or *16c-8a* transitions during the MD simulation,  $N$  the total number of Li-ions in the supercell and  $t$  the total simulation time. The respective activation

barriers for the *8a-16c* and *16c-8a* interface transitions are calculated using transition state theory by  $E_a = -kT \ln(\nu/\nu_0)$  <sup>[24]</sup> where  $\nu_0$  represents the attempt frequency, typically assumed to be  $10^{13}$   $\text{sec}^{-1}$  <sup>[25]</sup>,  $k$  is Boltzmann's constant and  $T$  the temperature, the results of which are presented in Table 1.

Composition	$T$ (K)	$t$ (ps)	Equilibration	Threshold	$E$ (eV)	$E$ (eV)
			Time (ps)	Time (ps)	<i>8a</i> $\rightarrow$ <i>16c</i>	<i>16c</i> $\rightarrow$ <i>8a</i>
A:Li <sub>5.2</sub> Ti <sub>5</sub> O <sub>12</sub>	520	185	3	0.1	<b>0.28</b>	<b>0.28</b>
A:Li <sub>5.2</sub> Ti <sub>5</sub> O <sub>12</sub>	520	185	<b>100</b>	0.1	<b>0.31</b>	<b>0.31</b>
A:Li <sub>5.2</sub> Ti <sub>5</sub> O <sub>12</sub>	<b>600</b>	<b>70</b>	3	0.1	<b>0.30</b>	<b>0.31</b>
B:Li <sub>5.7</sub> Ti <sub>5</sub> O <sub>12</sub>	600	<b>54</b>	3	0.1	<b>0.29</b>	<b>0.29</b>

**Table 1.** Activation energies of the *8a-16c* and *16c-8a* transitions resulting from various MD simulations where  $t$  is the total simulation time

The equilibration time has little influence on the calculated energy barriers as shown in **Table 1**. The energy barriers are slightly increasing when the equilibration time is increased to 100 ps where the MSD starts to flatten (**Figure 7c**). As expected for a system near equilibrium the barriers for *8a-16c* and *16c-8a* transition are symmetric, and they are in good agreement with NMR experiments <sup>[5, 6b, 12a, b]</sup> as well as with static DFT calculations based on the Nudged Elastic Band (NEB) approach <sup>[13, 14]</sup>. To examine whether the results depend on the starting conditions of the MD simulations or on temperature several simulations were performed, giving very similar results as shown in Table 1 and the **Supporting Information F. Figure 8** presents an overview of reported activation energies in literature, including the present results. Compared to the static

NEB calculations<sup>[13, 14]</sup>, based on non-stoichiometric cells, the MD simulations have the advantage to include the lattice kinetics and to give insight in the timescale of the most probable transitions. **Figure 8** indicates that high Li-ion mobility is expected for intermediate compositions,  $0 < x < 3$  in  $\text{Li}_{4+x}\text{Ti}_5\text{O}_{12}$ . The present results show that this is due to the  $\text{Li}^{16d}$  stabilized  $\text{Li}^{8a}$ - $\text{Li}^{16c}$  nearest neighbors which induce interfaces between the  $\text{Li}^{8a}$  and  $\text{Li}^{16c}$  domains with partially filled sites allowing facile Li-ion transitions. In contrast, the vacant sites in the endmembers (16c sites in  $\text{Li}_4\text{Ti}_5\text{O}_{12}$  and 8a sites in  $\text{Li}_7\text{Ti}_5\text{O}_{12}$ ) are unstable due to occupancy of all nearest neighbors. As a consequence there are effectively no vacancies to facilitate Li-ion diffusion resulting in the high activation energies observed and predicted<sup>[5, 6b, 12a, b, 13, 14]</sup>.

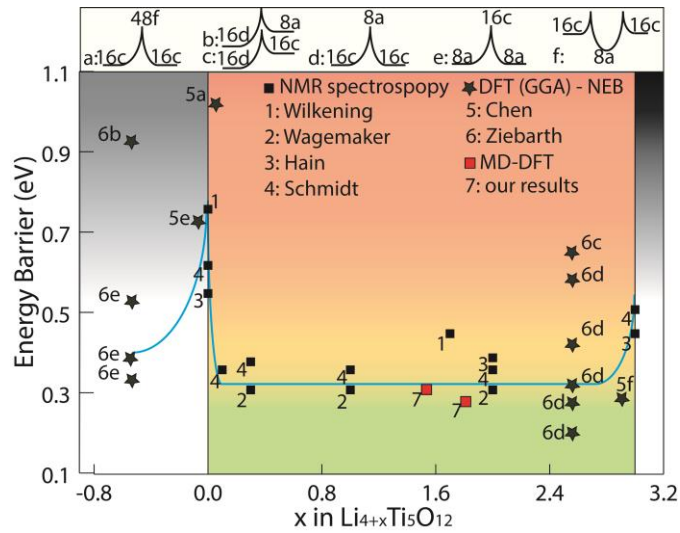


**Figure 8** Overview of the activation energy for Li-ion diffusion in spinel  $\text{Li}_{4+x}\text{Ti}_5\text{O}_{12}$  as a function of concentration, where the blue line represents the weighted average.

Considering the MSD during the first 100 ps equilibration time, a self-diffusion coefficient ( $D$ ) can be determined using  $D = \text{MSD}/(2Nt)^{[26]}$  where  $N$  is the dimensionality of the diffusion (in this case  $N = 3$  for the 3D diffusional work demonstrated by **Figure 7**), and  $t$  the time, resulting in  $D = 7.3 \cdot 10^{-7} \text{ cm}^2/\text{s}$  at 520 K. One could argue whether during the equilibration,

where there is a driving force towards a lower energy state, this can be considered to be a self-diffusion coefficient. However, given the very small energy gain during the simulation,  $\sim 0.021$  eV per Li-ion, we suggest that this is a realistic prediction of the self-diffusion coefficient. Given the calculated activation energy, see **Table 1**, this results in a room temperature self-diffusion coefficient of  $D = 7.5 \cdot 10^{-9} \text{ cm}^2/\text{s}$  which is in the upper range of chemical diffusion coefficients reported by electrochemical methods<sup>[8d, 15d]</sup>. However, it should be realized that, in particular for non-dilute systems such as LTO, the chemical and self-diffusion coefficients may differ considerably. The MSD obtained from the 70 ps calculation at 600 K results in a self-diffusion coefficient of  $D = 8.3 \cdot 10^{-7} \text{ cm}^2/\text{s}$  which at room temperature amounts to  $D = 3 \cdot 10^{-9} \text{ cm}^2/\text{s}$ , which is of the same order of magnitude as the MD simulation at 520 K.

To gain insight in this very high Li-ion mobility the local interface configurations and Li-ion transitions during the MD simulations are studied to highlight the origin of the high Li-ion conductivity of spinel  $\text{Li}_{4+x}\text{Ti}_5\text{O}_{12}$ . This results in three distinct interface configurations between which the system fluctuates as will be illustrated by the snap-shots of an MD simulation showing a typical evolution of the interface region in **Figure 9a-f**. **Figure 9** is a 2D projection of the 3D 8a and 16c site configuration on the  $xz$  plane, covering  $8.3 \text{ \AA}$  of depth in the  $y$ -direction, also indicating the  $\text{Li}^{16d}$  atoms nearest to the shown 8a and 16c sites as well as a schematic indication of the phase boundary. The starting frame, **Figure 9a**, depicts two of the three possible local interface configurations that occur during the simulations. For local configuration type 1 an occupied  $\text{Li}^{8a}$  site ( $\text{Li}_2$ ) has only one out of four nearest  $\text{Li}^{16c}$  ( $\text{Li}_3$ ) sites occupied. The resulting  $\text{Li}^{8a} - \text{Li}^{16c}$  nearest neighbor pair is stabilized by the neighboring  $\text{Li}^{16d}$ , representing the type of configuration shown in **Figure 3** that were found to have the lowest formation energy. The thermal fluctuations during the MD simulation result in a  $\text{Li}^{8a} - \text{Li}^{16c}$  nearest neighbor distance

between 2.2 and 2.7 Å, mediated by the relaxation near the  $Li^{16d}$ , consistent with the relaxation results that predict a value close to 2.4 Å (**Figure 3c,d,e**). This configuration allows several possible transitions as indicated by the straight dashed lines in **Figure 9a**. Local configuration type 2 is characterized by empty  $8a$  and  $16c$  sites at the interface between the  $Li^{8a}$  and  $Li^{16c}$  domains forming a (100) or (001) boundary (and (010) in 3D), see for instance near  $Li_4$  and  $Li_5$  in **Figure 9a**. The straight solid line in **Figure 9b** indicates an actual  $8a$ - $16c$  transition during the simulation, creating a new  $Li^{8a}$  -  $Li^{16c}$  nearest neighbor ( $Li_2$  and  $Li_7$ ), having interface configuration type 1, stabilized by the nearest  $Li^{16d}$ . This is followed by an  $8a$  to  $16c$  transition ( $Li_7$ ) in **Figure 9c** resulting in configuration type 2. The transitions from **Figure 9c** to **9e** proceed via another type 1 interface configuration, characterized by the  $Li^{8a}$  -  $Li^{16c}$  nearest neighbor pair, indicated with a red arrow in **Figure 9**. The sequence from **Figure 9a** to **9e** effectively causes the interface between the  $Li^{8a}$  and  $Li^{16c}$  domains to move, responsible for the dynamic domains structure shown in **Figure 7**, to reach the final interface configuration type 3 depicted in **Figure 9f** that occurs several pico-seconds later. In this interface type a diagonal empty layer of  $16c$  sites exist between the two phases (area between  $Li_3, Li_9, Li_4$ ). To transform this type 3 interface into a type 1 or 2 requires either a number of type 1 and type 2 transitions, or a  $16c$ - $8a$ - $16c$  transition which in this case actually occurs during the simulations, as indicated in **Figure 9f**, the result of which is again a type 1 interface configuration. This type of transition occurs approximately only 1 out of 100 transitions, the small probability of which is a consequence of the energetically unfavorable  $8a$  occupancy by the  $Li_9$  atom having two nearest  $Li^{16c}$  neighbors and no adjacent stabilizing  $Li^{16d}$ . The poor stability of the intermediate state of this transition is illustrated by its short 0.01 ps life time compared to the typical life time of the configurations shown in **Figure 9** which is generally more than 0.1 ps. This explains why  $16c$ - $8a$  transitions in  $Li^{16c}$  domains and

$8a-16c$  transitions in  $\text{Li}^{8a}$  domains are energetically very unfavorable and do not occur during the present MD simulations, consistent with NMR experiments<sup>[6b, 12a, b]</sup> and static DFT calculations<sup>[13, 14]</sup>. The transitions from **Figure 9b** to **9e** is completed within 0.4 ps indicating that the transitions at the interface may be strongly correlated. In order to investigate if the supercell size in the  $y$ -direction influences the result, a  $2 \times 2 \times 2$  supercell was simulated. Although the size of this supercell limits the total simulation time to 10 ps a number of similar correlated transitions were observed, indicating that these transitions are not induced by the periodic boundary conditions. Analyzing the interface configurations during the MD simulations reveals that adjacent type 1 configurations as well as adjacent type 1 and type 2 configurations are avoided, and that preferably a mixture of type 1 and type 2 or type 3 configurations is formed. This explains the equilibration during the MD simulations shown in **Figure 6** where the middle interface exists of adjacent type 2 configurations, and the interface at the bottom of the supercell, which is connected to the top, exists of adjacent type 1 configurations. This unfavorable situation relaxes during the MD simulation to a mixture of interface types as illustrated by the transitions during the initial stages of the MD simulations in **Supporting Information G**. During as well as after the equilibration, of approximately 100 ps, as shown in **Figure 8**, the same type of fluctuations between the three interface configurations are observed. The only difference is that the non-equilibrium conditions during the initial 100 ps cause a higher calculated transition frequency, responsible for the slightly lower energy barriers during the equilibration time in **Table 1**.

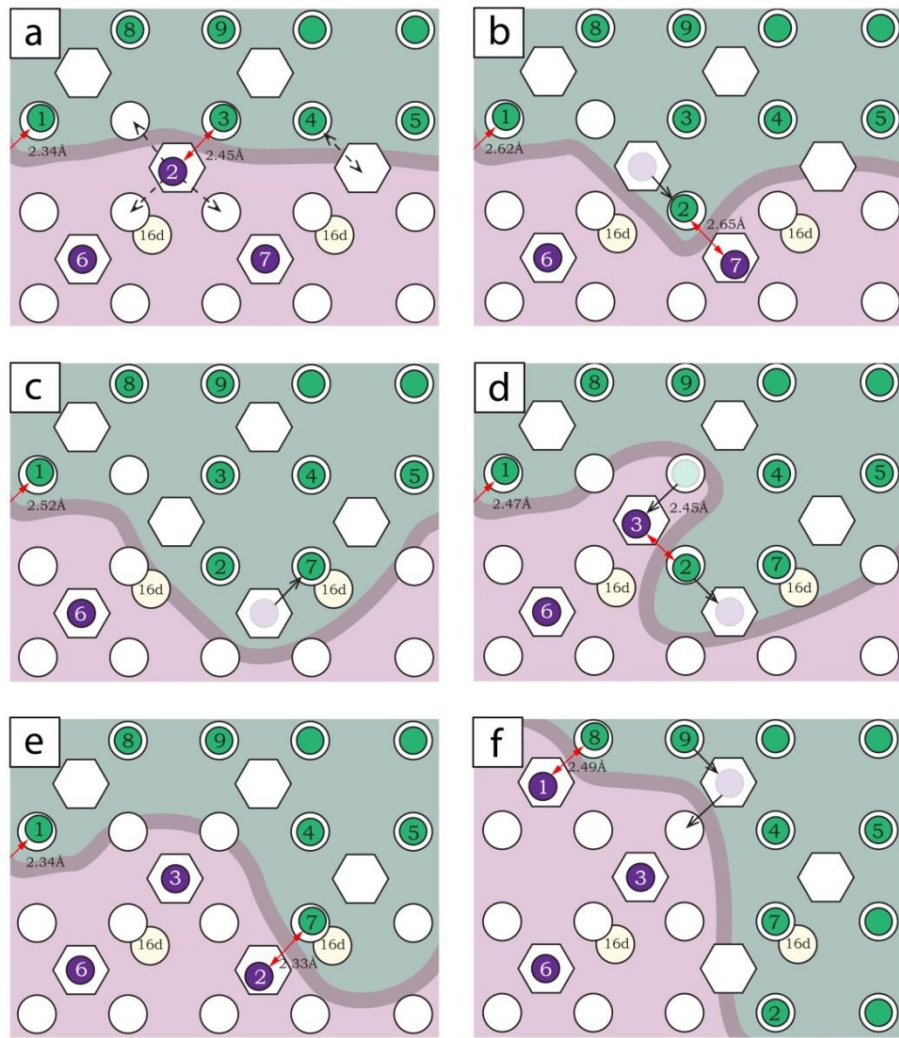


**Figure 9** Schematic 2D representation of the evolution of the 3D 8a and 16c site configuration during a sequence of snap-shots (during 5 ps) resulting from the Molecular Dynamics simulations ( $2 \times 1 \times 2$   $\text{Li}_{5.2}\text{Ti}_5\text{O}_{12}$ , 520 K). The hexagons represent the tetrahedral 8a sites and the circles represent the octahedral 16c sites. The color of the enumerated Li-ions (smaller circles) reflect the type of site they occupy, purple for 8a and green for 16c. The Li-ions residing at the 16d sites are indicated with a small offset in the xz plane making them visible behind the 16c sites but their distance to the two nearest 8a sites is equal. A schematic boundary is drawn

*separating the Li-poor ( $\text{Li}^{8a}$ ) and Li-rich ( $\text{Li}^{16c}$ ) domains . As indicated in **Figure 9** only diagonal transitions can occur connecting 8a sites via a 16c site and vice versa.*

The described mechanism demonstrates the crucial role of the  $\text{Li}^{16d}$  sites which locally stabilize type 1 interface configurations consistent with the most stable configurations in **Figure 3**. Because the  $\text{Li}^{16d}$  sites prefer to be well distributed through the lattice (**Figure 1**), with an average distance between 5.146 Å and 6.642 Å, this facilitates an abundance of interfaces. The MD simulations indicate that this results in  $\text{Li}^{8a}$  and  $\text{Li}^{16c}$  domain sizes as small as 1 nm in diameter, although the restricted supercell may influence this. The intimate mixing of the  $\text{Li}^{8a}$  and  $\text{Li}^{16c}$  domains is consistent with the recently observed percolating endmember phase mixture<sup>[27]</sup>. Moreover, the associated distribution in local configurations explain the local NMR observations<sup>[6b]</sup> and temperature dependent diffraction<sup>[6a]</sup> suggesting nanometer scale domains or even a complete solid solution<sup>[5]</sup>. Nevertheless the predicted sub-nanometer morphology represents a true first-order phase transition, as the chemical potential, the first derivative of the Gibbs free energy, is discontinuous as observed in **Figure 3d**. Solid solution like phases are experimentally observed in materials that are chemically lithiated. We anticipate that under the high-rate like conditions, associated with chemical lithiation, many particles react concurrently resulting in many particles that are partially lithiated in which the sub-nano morphology will establish. In contrast, relatively slow electrochemical lithiation is likely to activate only a small amount of grains leading to a macroscopic separation of the phases over different grains. This long-range phase separation may prevent reaching the equilibrium conditions described at present rendering the macroscopic phase separation a metastable condition, which explains the experimental observations of macroscopic phase separation<sup>[7a, b, 9]</sup>.

The  $Li^{16d}$  stabilized local interface configurations facilitate the high Li-ion mobility observed in the MD simulations, causing transitions between the type 1-3 interface configurations described in **Figure 9**. The high Li-ion mobility at the domain interfaces is responsible for the high mobility of the domain interface-morphology as observed in **Figure 6**, even at equilibrium conditions. Therefore we conclude that the high mobility of the Li-ions at the interface is responsible for the excellent conductivity of spinel  $Li_{4+x}Ti_5O_{12}$ . In addition, the interfaces are most likely responsible for the increased electronic conductivity observed<sup>[27, 28a, b, c]</sup> during battery cycling as they introduce a more homogeneous distribution of the mixed  $Ti^{+4}/Ti^{+3}$  oxidation states, which were recently shown by electrochemical and spectroscopic tools<sup>[28a]</sup> to be responsible for enhancing electronic transport. (De)lithiation of the endmember phases introduces the highly mobile interfaces that effectively activate the material by introducing high ionic and electronic mobility, consistent with experimental observations<sup>[5, 6b, 15d, 27, 28a, b, c]</sup>. Therefore the presence of the interfaces allows the system to respond very fast to non-equilibrium conditions occurring in Li-ion batteries, explaining the excellent rate capabilities of spinel  $Li_{4+x}Ti_5O_{12}$ .

### 3 Conclusions

Evaluation of the lowest energy configurations predicted by DFT calculations provides fundamental insight into the role of the  $Li^{16d}$  sites in disordered spinel  $Li_{4+x}Ti_5O_{12}$ . The  $Li^{16d}$  ions energetically prefer to be well distributed through the LTO lattice, and stabilize the adjacent nearest  $Li^{8a}$  -  $Li^{16c}$  neighbors. This in contrast to pure spinel  $Li_{1+x}Ti_2O_4$  where  $Li^{8a}$ - $Li^{16c}$  nearest neighbors are energetically highly unfavorable inducing macroscopic phase separation. In spinel  $Li_{4+x}Ti_5O_{12}$  the stabilization of  $Li^{8a}$  -  $Li^{16c}$  nearest neighbors allows intimate mixing of the  $Li^{8a}$  and  $Li^{16c}$  domains explaining both the solid solution interpretations and the observation of

domain structures. It represents, however, a true thermodynamic first-order phase transition consistent with the observed flat potential profile. The  $Li^{16d}$  stabilized  $Li^{8a}$  -  $Li^{16c}$  nearest neighbors also play a pivotal role in the kinetics of the system as illustrated by the Molecular Dynamics simulations, by allowing facile transitions between a few stable local interface configurations. These transitions induce rapidly moving interfaces between the  $Li^{8a}$  and  $Li^{16c}$  domains, explaining the very fast response on non-equilibrium conditions such as those occurring in Li-ion batteries. Thereby, unlike in other known first-order electrode materials, the low energy associated with the coexisting phases, makes that the phase separation in LTO appears to occur spontaneously towards sub-nanometer domains. This suggests that the first-order phase transformation appears to be driven by spinodal decomposition rather than nucleation. The simulations in this work suggest that it is this local environment that is responsible for the excellent rate performance and cycle life of spinel  $Li_{4+x}Ti_5O_{12}$  as Li-ion battery electrode. Nevertheless, it is possible that macroscopic phase separation can occur under non-equilibrium conditions during battery operation as the inter particle diffusion over large distances may prevent reaching the equilibrium conditions described at present, rendering macroscopic phase separation a metastable condition. Thereby the detailed local environment as described by the present DFT calculations brings forward a consistent understanding of the thermodynamics and kinetics of the spinel  $Li_{4+x}Ti_5O_{12}$  Li-ion battery electrode material.

## Methods

**Computational details** Calculations were performed using the Vienna *ab initio* simulation package (VASP)<sup>[29]</sup>

wherein the ground state energies were determined by the use of the generalized gradient approximation (GGA) to density functional theory (DFT).<sup>[16a, b, c]</sup> To describe the electron-ion-core interactions the projector augmented method (PAW)<sup>[30a, b]</sup> was used. The cutoff was set to 400 eV for accurate calculations. The total energy convergence was ensured to be within  $10^{-4}$  eV per formula unit between successive iterations with respect to the  $k$ -point sampling. For the MD simulations a  $k$ -point mesh of  $4 \times 4 \times 4$  was applied for supercell relaxations and total energy calculations. The  $k$ -point mesh was reduced to  $1 \times 1 \times 1$  for the MD simulation to ensure feasible computational times. The cutoff energy was set to 400 eV and a 2 fs time step appeared appropriate for the simulations. To determine the position of the mobile Li-ions during the MD simulations the distance of the Li-ions from the crystallographic sites in LTO<sup>[26]</sup> were monitored. A Li-ion within a radius of 0.8 Å from the crystallographic positions was interpreted as occupying the specific position. A variety of threshold and equilibration times were applied to test the consistency in the hopping time scales. Finally, visualization tools (Material Studio and Mat lab) were used to derive the macroscopic and microscopic pictures of the moving interface.

**The insertion voltage** The difference in Gibbs free energy  $\Delta G$  for the Li insertion reaction can be used to determine the average voltage for Li insertion as<sup>[31]</sup>

$$\bar{V} = \frac{-\Delta G}{(x_2 - x_1)F},$$

where  $x_1$  and  $x_2$  are the two end Li-compositions between which insertion occurs ( $x_2 > x_1$ ) and  $F$  is Faradays constant. This is further simplified by the assumption that the changes that occur in volume and entropy are very small during this reaction as a result of which the average insertion voltage can be approximated to

$$\bar{V} = \frac{-\Delta E}{(x_2 - x_1)F},$$

where  $\Delta E$  is the calculated total energy difference of the two Li-composition limits taking metallic Li as a reference.

## Acknowledgements

We would like to acknowledge financial support from NWO-NANO for SG. The research leading to these results has received funding from the European Research Council under the European Union's Seventh Framework Program (FP/2007-2013) / ERC Grant Agreement no. [307161] of MW.

## References

- [1] A. K. Padhi, K. S. Nanjundaswamy, J. B. Goodenough, *J. Electrochem. Soc.* **1997**, *144*, 1188.
- [2] a) A. Deschanv, B. Raveau, Z. Sekkal, *Mater. Res. Bull.* **1971**, *6*, 699; b) K. M. Colbow, J. R. Dahn, R. R. Haering, *J. Power Sources* **1989**, *26*, 397.
- [3] a) Y. Orikasa, T. Maeda, Y. Koyama, H. Murayama, K. Fukuda, H. Tanida, H. Arai, E. Matsubara, Y. Uchimoto, Z. Ogumi, *J. Am. Chem. Soc.* **2013**, *135*, 5497; b) Y. Orikasa, T. Maeda, Y. Koyama, H. Murayama, K. Fukuda, H. Tanida, H. Arai, E. Matsubara, Y. Uchimoto, Z. Ogumi, *Chem. Mater.* **2013**, *25*, 1032.
- [4] a) X. Zhang, M. van Hulzen, D. P. Singh, A. Brownrigg, J. P. Wright, N. H. van Dijk, M. Wagemaker, *Nano Lett.* **2014**, *14*, 2279; b) P. Bai, D. A. Cogswell, M. Z. Bazant, *Nano Lett.* **2011**, *11*, 4890; c) D. A. Cogswell, M. Z. Bazant, *ACS Nano* **2012**, *6*, 2215; d) X. Zhang, M. van Hulzen, D. P. Singh, A. Brownrigg, J. P. Wright, N. H. van Dijk, M. Wagemaker, *Nat. Commun.* **2015**, *6*; e) H. Liu, F. C. Strobridge, O. J. Borkiewicz, K. M. Wiaderek, K. W. Chapman, P. J. Chupas, C. P. Grey, *Science* **2014**, *344*; f) M. Hess, T. Sasaki, C. Villevieille, P. Novak, *Nat. Commun.* **2015**, *6*.
- [5] W. Schmidt, P. Bottke, M. Sternad, P. Gollob, V. Hennige, M. Wilkening, *Chem. Mater.* **2015**, *27*, 1740.
- [6] a) M. Wagemaker, D. R. Simon, E. M. Kelder, J. Schoonman, C. Ringpfeil, U. Haake, D. Lützenkirchen-Hecht, R. Frahm, F. M. Mulder, *Adv. Mater.* **2006**, *18*, 3169; b) M. Wagemaker, E. R. H. van Eck, A. P. M. Kentgens, F. M. Mulder, *J Phys Chem B* **2009**, *113*, 224; c) X. Lu, L. Zhao, X. Q. He, R. J. Xiao, L. Gu, Y. S. Hu, H. Li, Z. X. Wang, X. F. Duan, L. Q. Chen, J. Maier, Y. Ikuhara, *Adv. Mater.* **2012**, *24*, 3233.
- [7] a) S. Scharner, W. Weppner, P. Schmid-Beurmann, *J. Electrochem. Soc.* **1999**, *146*, 857; b) M. Kitta, T. Akita, S. Tanaka, M. Kohyama, *J. Power Sources* **2014**, *257*, 120.
- [8] a) T. Ohzuku, A. Ueda, N. Yamamoto, *J. Electrochem. Soc.* **1995**, *142*, 1431; b) D. C. Johnston, *J. Low Temp. Phys.* **1976**, *25*, 145; c) E. Ferg, R. J. Gummow, A. Dekock, M. M. Thackeray, *J. Electrochem. Soc.* **1994**, *141*, L147; d) L. Kavan, M. Gratzel, *Electrochem. Solid State Lett.* **2002**, *5*, A39.

- [9] S. Tanaka, M. Kitta, T. Tamura, Y. Maeda, T. Akita, M. Kohyama, *J. Mater. Sci.* **2014**, *49*, 4032.
- [10] M. Wagemaker, W. J. H. Borghols, F. M. Mulder, *J. Am. Chem. Soc.* **2007**, *129*, 4323.
- [11] M. Wagemaker, F. M. Mulder, A. van der Ven, *Adv. Mater.* **2009**, *21*, 1.
- [12] a) M. Wilkening, W. Iwaniak, J. Heine, V. Epp, A. Kleinert, M. Behrens, G. Nuspl, W. Bensch, P. Heitjans, *Phys. Chem. Chem. Phys.* **2007**, *9*, 6199; b) H. Hain, M. Scheuermann, R. Heinzmann, L. Wunsche, H. Hahn, S. Indris, *Solid State Nucl. Mag.* **2012**, *42*, 9.
- [13] Y. C. Chen, C. Y. Ouyang, L. J. Song, Z. L. Sun, *Electrochim. Acta* **2011**, *56*, 6084.
- [14] B. Ziebarth, M. Klinsmann, T. Eckl, C. Elsasser, *Phys. Rev. B* **2014**, 89.
- [15] a) Y. H. Rho, K. Kanamura, *J. Solid State Chem.* **2004**, *177*, 2094; b) K. Zaghib, M. Simoneau, M. Armand, M. Gauthier, *J. Power Sources* **1999**, *81*, 300; c) S. Bach, J. P. Pereira-Ramos, N. Baffier, *J. Power Sources* **1999**, *81*, 273; d) L. Kavan, J. Prochazka, T. M. Spitler, M. Kalbac, M. T. Zikalova, T. Drezen, M. Gratzel, *J. Electrochem. Soc.* **2003**, *150*, A1000; e) N. Takami, K. Hoshina, H. Inagaki, *J. Electrochem. Soc.* **2011**, *158*, A725.
- [16] a) P. Hohenberg, W. Kohn, *Phys. Rev.* **1964**, *136*, B864; b) J. P. Perdew, K. Burke, Y. Wang, *Phys. Rev. B* **1996**, *54*, 16533; c) J. P. Perdew, J. A. Chevary, S. H. Vosko, K. A. Jackson, M. R. Pederson, D. J. Singh, C. Fiolhais, *Phys. Rev. B* **1992**, *46*, 6671.
- [17] J. Bhattacharya, A. Van der Ven, *Phys. Rev. B* **2010**, 81.
- [18] a) A. Van der Ven, M. K. Aydinol, G. Ceder, G. Kresse, J. Hafner, *Phys. Rev. B* **1998**, *58*, 2975; b) A. Van der Ven, G. Ceder, *Phys. Rev. B* **1999**, *59*, 742; c) A. Van der Ven, C. Marianetti, D. Morgan, G. Ceder, *Solid State Ion.* **2000**, *135*, 21.
- [19] M. Wagemaker, A. Van Der Ven, D. Morgan, G. Ceder, F. M. Mulder, G. J. Kearley, *Chem. Phys.* **2005**, *317*, 130.
- [20] Z. Y. Zhong, C. Y. Ouyang, S. Q. Shi, M. S. Lei, *ChemPhysChem* **2008**, *9*, 2104.
- [21] W. J. H. Borghols, M. Wagemaker, U. Lafont, E. M. Kelder, F. M. Mulder, *J Am Chem Soc* **2009**, *131*, 17786.
- [22] H. Ge, N. Li, D. Y. Li, C. S. Dai, D. L. Wang, *Electrochem. Commun.* **2008**, *10*, 719.
- [23] a) A. R. Armstrong, C. Lyness, P. M. Panchmatia, M. S. Islam, P. G. Bruce, *Nat. Mater.* **2011**, *10*, 223; b) Y. S. Meng, M. E. Arroyo-de Dompablo, *Energy Environ. Sci.* **2009**, *2*, 589.
- [24] G. H. Vineyard, *J. Phys. Chem. Solids* **1957**, *3*, 121.
- [25] A. Van der Ven, G. Ceder, M. Asta, P. D. Tepesch, *Phys. Rev. B* **2001**, 64.
- [26] M. W. Niek J. J. de Klerk, *Chem. Mater.* **2016**.
- [27] M. G. Verde, L. Baggetto, N. Balke, G. M. Veith, J. K. Seo, Z. Y. Wang, Y. S. Meng, *ACS Nano* **2016**, *10*, 4312.
- [28] a) C. Kim, N. S. Norberg, C. T. Alexander, R. Kostecki, J. Cabana, *Adv. Funct. Mater.* **2013**, *23*, 1214; b) D. Young, A. Ransil, R. Amin, Z. Li, Y. M. Chiang, *Adv. Energy Mater.* **2013**, *3*, 1125; c) M. S. Song, A. Benayad, Y. M. Choi, K. S. Park, *Chem. Commun.* **2012**, 48, 516.
- [29] G. Kresse, J. Furthmüller, *Phys. Rev. B* **1996**, *54*, 11169.
- [30] a) P. E. Blochl, *Phys. Rev. B* **1994**, *50*, 17953; b) G. Kresse, D. Joubert, *Phys. Rev. B* **1999**, *59*, 1758.
- [31] M. K. Aydinol, A. F. Kohan, G. Ceder, K. Cho, J. Joannopoulos, *Phys. Rev. B* **1997**, *56*, 1354.

# Table of contents graphic (TOC)

